A hierarchical Si_{PN}/CN/MoS_x photocathode with low internal resistance and strong light-absorption for solar hydrogen production

Shenfeng Zhang [a,1], Hui Zhao [a,b,1], Xin Li [a,1], Ying Li [a,*], Yuebo Jin [a], Xuefeng Liu [a], Gang Shi [a,*], Po Keung Wong [b,c,**]

[a] *The Key Laboratory of Synthetic and Biotechnology Colloids, Ministry of Education, School of Chemical and Material Engineering, Jiangnan University, 1800 Lihu Avenue, Wuxi 214122, China*
[b] *School of Life Sciences, The Chinese University of Hong Kong, Shatin, NT, Hong Kong, SAR, China*
[c] *Institute of Environmental Health and Pollution Control, School of Environmental Science & Engineering, Guangdong University of Technology, Guangzhou 510006, China*

ARTICLE INFO

ABSTRACT

The Si/MoS_x photocathode is usually fabricated by electrochemical deposition, which high interfacial resistance is usually solved by building a buried junction or inserting a metal layer between Si and MoS_x. Both methods, however, involve toxic gas sources or harsh conditions of high pressure. Here, a green and mild route has been designed to insert the N-doped carbon (CN) layer between Si and MoS_x by in situ polymerization and post-annealing, which improves the transfer of interfacial carriers and avoids unnecessary absorption of incident light by itself. Meanwhile, combining two-step wet etching and photo-assisted electro-deposition, the Si_{PN}/CN/MoS_x photocathode with antireflective structure was obtained.

The Si_{PN}/CN/MoS_x hybrid photocathode shows excellent performance (0.23 V onset potential and 10 $mA·cm^{-2}$ photocurrent at 0 V vs RHE in 0.5 MH_2SO_4 under the condition of simulated sunlight). The design of Si_{PN}/CN/MoS_x photocathode will provide a new idea for PEC water splitting.

1. Introduction

Photoelectrochemical (PEC) water splitting is currently one of the most promising methods for producing hydrogen [1–7]. Among them, the photocathode composed of molybdenum sulfide (MoS_x) and monocrystalline silicon (Si) has attracted extensive concern [8–13]. Because Si is an ideal photocathode semiconductor material with a suitable optical band gap (1.1 eV), and it can absorb light with a wavelength of less than 1100 nm in the solar spectrum [14–19]. At the same time, MoS_x with the characteristics of cheap and non-toxic, as a hydrogen evolution reaction HER promoter [20–29], can improve the problem of slow reaction kinetics on the Si surface. For example, Jihun Oh et al. developed an efficient Si/MoS_2 photocathode by using the ALD method to directly grow MoS_2 on the Si surface [30]. Song Jin et al. prepared $Si/1T-MoS_2$ photocathode by CVD [31]. Jinhua Ye et al. prepared $Si/a-MoS_x$ photocathode by HF chemical reduction method [32]. These works have

shown that the combination of MoS_x and Si can construct a photocathode with excellent PEC performance.

In addition to the above methods, the electrochemical deposition technology for fabricating $Si-MoS_x$ composite photocathode has attracted much attention. Electrodeposition does not require high-temperature and high-energy processes, which avoids damage to semiconductor materials during the fabricating process. However, the Si substrate has poor conductivity, and only a little amount of electrons moves directionally under the force of an electric field. It is difficult to achieve the reduction and deposition of the cathode to obtain MoS_x. In order to solve the above problems, the photo-assisted electrodeposition was introduced into the process of fabricating MoS_x on the surface of Si. The advantage of this approach is that that a large number of electrons are produced from Si under illumination, and undergo directional movement under the force of an electric field, which can reduce the $[MoS_4]^{2-}$ on the Si surface into MoS_x in situ. The related works are listed

---

and compared in Table S1. For instance, Phong D. Tran et al. assembled MoS_2 on the surface of Si nanowires to form Si-NW/MoS_2 photocathode through metal-assisted chemical etching and photo-assisted electrode-position, which was found to be mechanically robust and stable without MoS_2 detachment even under ultrasonication conditions. But the onset potential of the photocathode is only 0 V vs RHE. The reason is that Si was corroded by the aqueous electrolyte during the photo-assisted electrodeposition process, and SiO_x was then generated at the inter-face of Si and MoS_2, hindering the interface transmission of photo-generated carriers [33]. In order to prevent the corrosion of the Si surface by the aqueous electrolyte, Michael J. Rose et al. used ionic liquid as the electrolyte to reduce the influence of dissolved oxygen in the solution on the substrate, which improved the onset potential (0.14 V vs RHE) of the Si/MoS_x photocathode [34]. However, there is still a large interface resistance at the interface of Si and MoS_x.

In the field of photo-assisted electrodeposition for Si-MoS_x, there are two most effective methods to reduce the interface resistance. One method is based on the buried junction, which is formed by preparing an n-type diffusion layer on the surface of p-Si [35,36]. The other method is based on the metal layer, which is inserted between MoS_2 and Si. The buried junction can form a built-in electric field from n→p in the bulk phase of Si, facilitating the outward migration of photogenerated car-riers. In addition, the metal interlayer can form a conductive metal silicide in the subsequent annealing process, which reduces the interface resistance of the outward migration of photogenerated carriers between MoS_2 and Si. For example, Ib Chorkendorff et al. builted the surface n^+p junction of p-Si through phosphorus doping from a gaseous $POCl_3$ at 900 °C, and then the inserted metal (Ti) at the heterogeneous interface of n^+p-Si/MoS_2 photocathode by magnetron sputtering [37]. The n^+p junction and inserted metal layer can improve the transport capability of carriers and enhance the stability, resulting in onset potential of 0.33 V vs RHE. Generally, the inserted metal layer is realized by magnetron sputtering, which requires harsh conditions of high vacuum and expensive equipment. The buried junction is usually realized by high temperature diffusion process, which requires poisonous $POCl_3$ as phosphorus source, and even requires harsh conditions with tempera-ture higher than 900 °C. In this way, it is worth considering how to reduce the interface resistance of Si/MoS_x photocathode and improve the photoelectric catalytic efficiency under the green and mild conditions.

N-doped carbon (CN) with graphene-like structure can increase conductivity and improve the interface compatibility between Si and MoS_x. It can also passivate the surface to reduce the probability of introducing defects during the photo-assisted electrodeposition process, and provide electrodeposition sites for MoS_x, thereby improving the stability of the photoelectrode. In addition, the thin CN layer has excellent optical transmittance, which can ensure that most of the light is absorbed by Si to generate photo-generated carriers. Therefore, a green and mild route of two-step wet etching, in situ polymerization and photo-assisted electro-deposition was designed to form bio-inspired photocathode, consisting of monocrystal Si with micro-pyramids and nano-pores (Si_{PN}), conductive N-doped carbon (CN) layer and MoS_x catalyst. The Si_{PN} can provide has a large specific surface area and a high light-harvesting ability, contributing to producing more photogenerated carriers. MoS_x as a catalyst can collect photogenerated carriers of Si and reduce their recombination, and thus enhance HER activity. The CN layer between MoS_x and Si_{PN} can increase conductivity, and improve the transfer of interfacial carriers.

2. Experimental section

2.1. Reagents and materials

Acetone, chloroform, ethanol, dopamine hydrochloride (DA), po-tassium hydroxide, trishydroxymethylaminomethane (THAM), sodium molybdate dihydrate, sodium sulfide nonahydrate, isopropyl alcohol

hydrochloric acid (37%) are all Analytical pure; all purchased from Sinopharm Group Chemical Reagent Co., Ltd.; The reagents are used without special treatment. The Si wafer is monocrystalline Si [P type (100)] purchased from Youyan Semiconductor Materials Co., Ltd.

2.2. Fabrication of Si_{PN}

Firstly, the Si wafer was cut into 1 cm × 1 cm and ultrasonic cleaned with deionized water for 5 min. Then, the Si wafer was etched to form micro-pyramid Si (Si_P) in KOH solution for 30 min at 85 °C [38,39]. Subsequently, Ag nanoparticles were deposited on Si_P in HF (4.8 M) solution with $AgNO_3$ (5 mM) for 1 min at 25 °C. Finally, Si_P with Ag nanoparticles was etched to form nano-pores (Si_{PN}) in HF (4.8 M) so-lution with H_2O_2 (4 mM) for 6 min at 25 °C [40].

2.3. Fabrication of Si_{PN}/CN

(1) PDA deposition: Si_{PN} was immersed into 30 mL buffer solution of THAM (0.01 mol), which contained DA hydrochloride (0.26 mol). The above solution was then slowly stirred with magnetic force at 30 °C for 100 min to form the PDA coating on Si_{PN} (Si_{PN}/PDA) by in-situ poly-merization of DA. (2) PDA carbonization: PDA was annealed at 500 °C for 2 h under N_2 atmosphere and was treated by 5% HF for 1 min, to form a nitrogen-doped carbon layer on Si_{PN} (Si_{PN}/CN) [41].

2.4. Fabrication of Si_{PN}/CN/MoS_x

(1) Preparation of sodium tetrathiomolybdate: 0.24 g of sodium molybdate and 0.96 g of sodium sulfide were dissolved into 80 mL of deionized water. Subsequently, 5% of HCl was dropped slowly until the above solution turned black-red. Then, the volume and pH value of the above solution were adjusted to 100 mL and 8. (2) Photo-assisted elec-trodeposition of MoS_x: 50 mL solution of sodium tetrathiomolybdate was taken as the electrolyte. Si_{PN}/CN, platinum (Pt) mesh and Ag/AgCl were used as the working electrode, the counter electrode and the reference electrode, respectively. Thus, MoS_x was deposited on Si_{PN}/CN to form Si_{PN}/CN/MoS_x by photo-assisted electrodeposition at a constant potential of −1 V vs RHE under AM 1.5 G illumination (100 mW·cm^{-2}) for 200 s [42].

2.5. Fabrication of Si_{PN}/MoS_x

Si_{PN}/MoS_x was fabricated by electrodepositing MoS_x on Si_{PN} instead of Si_{PN}/CN, which electrodeposition condition is the same to that in Section 2.4.

2.6. Characterizations

The structural characterization of the sample was carried out by scanning electron microscope (SEM, SITA HITACHI S-4800 (Japan) and ZEISS GEMINISEM360 (Germany)) with energy dispersive X-ray spec-troscopy (EDS) and. The ultraviolet-visible diffuse reflection spectrum of the sample was measured by the plus ultraviolet-visible near-infrared spectrophotometer (Shimadzu UV-3600, Japan). The photoelectric cat-alytic hydrogen production was measured by the electrochemical workstation (Shanghai Chenhua Company CHI660, China). The crystal structure of the sample was determined by the X-ray diffractometer (XRD, Bruker AXS D8, Germany). The valence state and electron transfer tests were performed using the Axis supra X-ray photoelectron spec-trometer (XPS, Axis supra, Kratos UK). The amount of hydrogen pro-duced was calibrated using the gas chromatograph (GC, Zhejiang Fuli Analytical Instrument GC9790plus, China). The calcination of the ma-terial was carried out by vacuum horizontal tube furnace (Shanghai Shengli Testing Instrument SLG1300–60, China).

2.7. Evaluation of photoelectric capability

The photo of the experimental setup for the evaluation of photo-electric capability has been shown in Fig. S7. A 300 W Xenon lamp was used as the excitation light source for the photoelectrochemical measurement experiment of $Si_{PN}/CN/MoS_x$. The power (100 mW·cm^{-2}) of incident light on the sample was accurately maintained, which was measured by a standard power meter. The single-component conductive silver glue and the copper on the back of the Si substrate provided ohmic contact. The entire sample was completely protected with epoxy resin. PEC was tested with $Si_{PN}/CN/MoS_x$, Pt mesh and Ag/AgCl as the working electrode, the counter electrode and the reference electrode respectively. All PEC tests were conducted in the voltage range of 0.4 to −0.6 V. The scan rate was 10 mV/s, the impedance measurement value was 1 Hz to 100 kHz, and the applied potential was 0 V vs RHE. The measurement was performed in a 0.5 M H$_2$SO$_4$ electrolyte solution so that the pH value was 0.3. The measurement temperature was accurately maintained at 25 °C, and all measured values were calibrated to $E_{RHE} = E_{Ag/AgCl} + E^0_{Ag/AgCl} + 0.0591 \times pH$, $E^0_{Ag/AgCl}$ (3 M KCl) = 0.197 V at 25 °C using the Nernst equation [43,44]. 0 V vs RHE is equivalent to − 0.215 V vs Ag/AgCl in this article.

The incident-photon-to-current-conversion efficiency (IPCE) values were determined by using the equation:

$$IPCE = \left[\frac{hv \times (J_{light} - J_{dark})}{e\lambda P_\lambda}\right] \qquad (1)$$

Where h is Planck constant, c is the speed of light in vacuum, λ is the light wavelength, J_{light}-J_{dark} is the net photocurrent density, e is the electronic elementary charge and P_λ is the incident light flux measured with a power meter.

Faradaic efficiency (FE) was calculated using the following equation:

$$FE\% = \frac{Hydrogen\ evolution\ measured}{\left(\frac{J_{ph} \times A \times t}{e}\middle/2\right)\middle/N_A} \times 100\% \qquad (2)$$

where J_{pH} is the current density (A·cm^{-2}), A is the area (cm^2), t is the time (s), e is the electronic elementary charge (1.602 $\times10^{-19}$ C), and N_A is the Avogadro number (6.02 $\times$ 10^{23} mol^{-1}) [5].

3. Results and discussion

3.1. Materials fabrication and surface characterization

The fabrication process of $Si_{PN}/CN/MoS_x$ photocathode is shown in Fig. 1. In the first place, the micro-pyramid Si (Si_P) was obtained by anisotropy etching in alkali solution. The morphology of Si_P is shown in Fig. 2a, with height of 3 μm and smooth sidewalls of 54.7°. The formation of micro-pyramids is due to that the KOH etching rate of Si (111) is ~30 times lower than that of Si (100) [45]. Then, nano-pores were constructed on Si_P (Si_{PN}) by metal catalytic etching in HF/H$_2$O$_2$ solution. According to the effective medium theory (EMT) [46,47], the micro-pyramids and nano-pores of Si_{PN} can slow down the change of the refractive index from air to substrate, which helps to reduce the reflection of incident light. Its excellent anti-reflective performance is shown in "3.2 optical properties characterization" and discussed in detail. The morphology of Si_{PN} is shown in Fig. 2b, which diameter and height of nano-pores are 150 and 800 nm, respectively. Subsequently, PDA was assembled on the surface of Si_{PN}. Fig. 2c shows the SEM image of Si_{PN} with PDA, which is derived from the in-situ polymerization of DA with strong adhesion. PDA is uniformly distributed with a particle size of ~10 nm, as shown in Fig. S1. The nitrogen-doped carbon (CN) [48] layer was then grown on Si_{PN} (Si_{PN}/CN) by annealing PDA, which can reduce the contact resistance between Si and MoS_x. Its morphology is shown in Fig. 2d, indicating that the CN layer has a relatively uniform distribution on the sidewall surface of the Si nano-pores. Finally, MoS_x was assembled on Si_{PN}/CN ($Si_{PN}/CN/MoS_x$) through the photo-assisted electrodeposition technology, which is uniformly distributed, as shown in Fig. 2e. MoS_x can collect photo-generated electrons and accelerate the rate of HER reaction. As shown in Fig. 2f with XRD patterns, the sharp peak at 2θ value of 69° is the diffraction peak of monocrystalline Si, and the broad peaks at 2θ value of 27° and 10°, correspond corresponding to the amorphous C and MoS_x, respectively. Thus, the $Si_{PN}/CN/MoS_x$ photocathode for hydrogen evolution has been
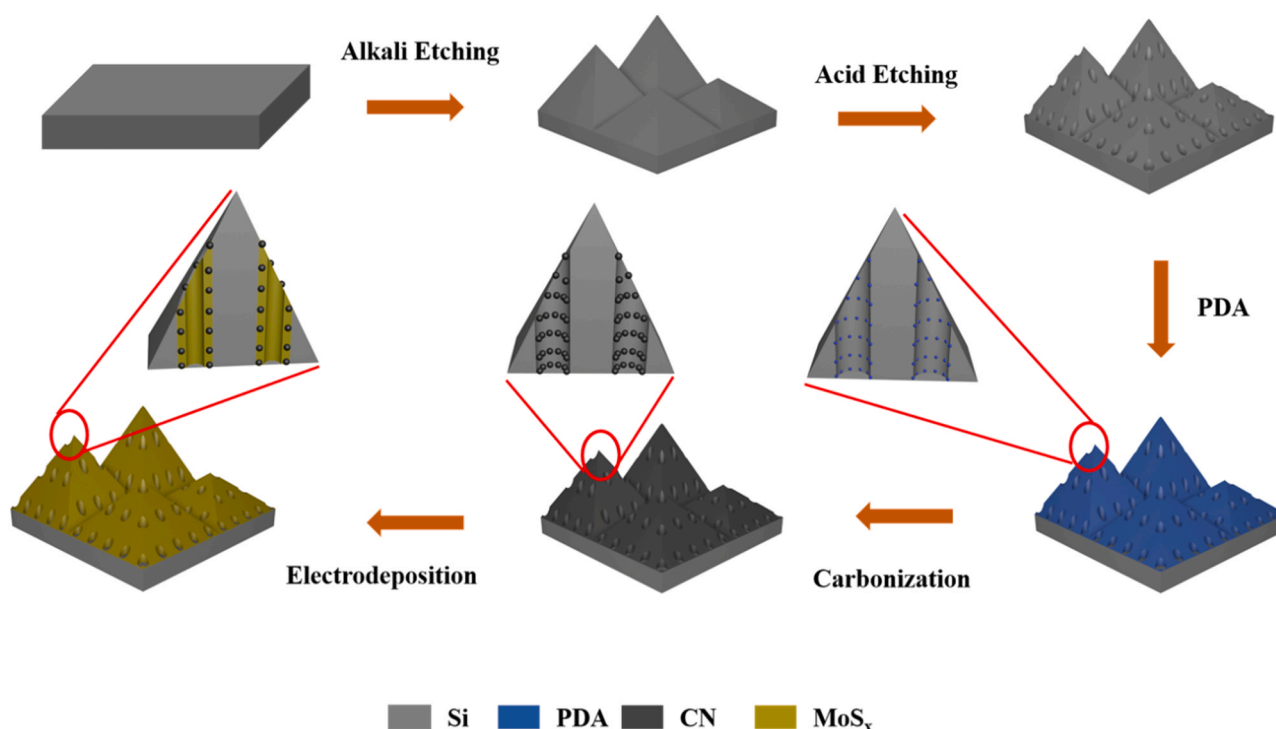

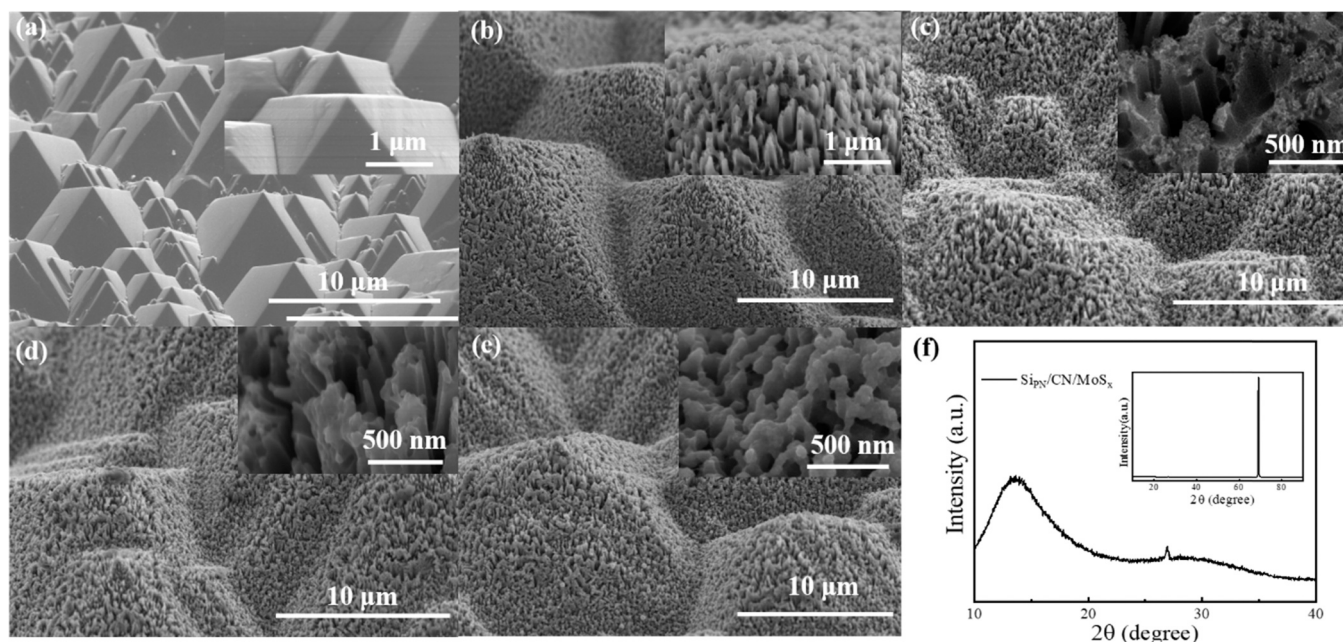**Fig. 1.** Schematic illustration of fabricating $Si_{PN}/CN/MoS_x$ photocathode.

Fig. 2. SEM images of (a) Si_P, (b) Si_{PN}, (c) Si_{PN}/PDA, (d) Si_{PN}/CN and (e) $Si_{PN}/CN/MoS_x$. Inset: zoomed view. (f) XRD pattern of $Si_{PN}/CN/MoS_x$.

successfully fabricated. Fig. 3 is EDS images showing the element distribution of Si, C, N, Mo and S, which indicates the uniform distribution of CN and MoS_x on Si_{PN}.

In particular, the CN layer is critical to the performance of the $Si_{PN}/$ CN/MoS_x photocathode for the following reasons. (1) The inserted CN layer with excellent conductivity can effectively transfer the photo-generated electrons generated by Si to the surface of MoS_x, which reduces the recombination probability of photogenerated electrons and holes and improves the photoelectric conversion efficiency of the $Si_{PN}/$ CN/MoS_x electrode. (2) The inserted CN layer with high transmittance (seeing Fig. S2) to incident light can ensure the effective light-absorption of the underlying Si substrate, increasing the number of photogenerated carriers and improving the photoelectric conversion efficiency of the electrode. (3) The inserted CN layer can improve the interfacial compatibility between Si and MoS_x, which prevents MoS_x from falling off the electrode. (4) The inserted CN layer can prevent Si from being oxidized by the electrolyte, improving the electrochemical stability of $Si_{PN}/CN/MoS_x$.

In order to further prove the distribution of the various components of the $Si_{PN}/CN/MoS_x$ photocathode, the SEM image with cross-sectional analysis of the $Si_{PN}/CN/MoS_x$ is shown in Fig. S3a. It is obvious that there are two areas on the surface of the Si substrate, namely area I and area II. According to the assembly sequence of the components in the sample, it is predicted that area I and area II are the CN layer and the MoS_x layer, respectively, and their corresponding average thicknesses are 8.6 nm and 30.9 nm, respectively. Meanwhile, Fig. S3b shows the SEM cross-sectional image of the Si_{PN} substrate with only CN layer. To further prove the above prediction, the elemental composition and bonding energy of MoS_x layer and CN layer on the surface of the $Si_{PN}/$ CN/MoS_x photocathode were respectively analyzed by XPS [49–51] combined with etching process, as shown in Fig. 4a-e. First of all, when the sample is not etched, there are Mo and S elements. Fig. 4b and Table S2 show that four binding energy (BE) peaks located at 229.90, 233.20, 232.50 and 235.60 eV represent Mo $3d_{5/2}$ orbital of Mo^{IV}, Mo $3d_{3/2}$ orbital of Mo^{IV}, Mo $3d_{5/2}$ orbital of Mo^{VI} and Mo $3d_{3/2}$ orbital of Mo^{VI}, respectively. Fig. 4c and Table S2 show that the BE peaks at 161.80 and 162.50 eV are attributed to the S $2p_{3/2}$ and S $2p_{1/2}$ orbitals of S^{2-}, and the BE peaks at 163.40 and 164.50 eV are attributed to the S $2p_{3/2}$ and S $2p_{1/2}$ orbitals of coordinated S_2^{2-}. Fig. 4c and Table S2 show that the BE peaks at 162.05 and 163.32 eV are attributed to the S $2p_{3/2}$

and S $2p_{1/2}$ orbitals of S^{2-}, which has lower HER activity. And the BE peaks at 163.10 and 164.50 eV are attributed to the S $2p_{3/2}$, S $2p_{1/2}$ orbitals of coordinated S_2^{2-}, which has higher HER activity [49,51]. The above analysis proves that the outer layer is MoS_x. In addition, it is found that there is C element at the same time, which was caused by the adsorption of a little amount of CO_2 and organic gases in the air on the surface of MoS_x. After the sample was etched for 2 min, the C element basically disappeared, and the relevant characteristic peaks of MoS_x still existed, further proving that the material in area II is MoS_x. After the sample was etched for another 60 min, the Mo and S elements disappeared, but the C and N elements appeared, as shown in Fig. 2a. At the same time, Fig. 4d shows that the BE peaks at 284.00, 284.80, 285.80, 286.60 and 288.60 eV, respectively correspond to the sp^2 C–C, sp^3 C–C, sp^2 C–N, sp^3 C–O and sp^3 C–N structures in the C 1 s region, respectively. In addition, Fig. 4e shows that the BE peaks at 398.70 and 400.10 eV correspond to the sp^3 C–N and sp^2 C–N structures in the N 1s region, respectively. The above analysis indicates that the lower part of the MoS_x layer was the CN layer, and further verifies the accuracy of the prediction for area I. In summary, the CN layer and MoS_x layer were assembled on the Si_{PN} surface in turn.

3.2. Optical properties characterization

Fig. 4f shows the reflectance spectrum of $Si_F/CN/MoS_x$, $Si_P/CN/$ MoS_x, $Si_{PN}/CN/MoS_x$ and Si_{PN}/MoS_x. The reflectance of $Si_F/CN/MoS_x$, $Si_P/CN/MoS_x$, $Si_{PN}/CN/MoS_x$ decreased in turn, as shown in curves (a)-(c). Among them, $Si_{PN}/CN/MoS_x$ has the lowest reflectivity, which is less than 6% in the wavelength range of 300–1100 nm. This sample showed excellent anti-reflection ability. This is due to that $Si_{PN}/CN/MoS_x$ has an excellent anti-reflective structure of micro-pyramid and nano-pores. According to EMT, the sudden change of refractive index from air to the substrate surface is reduced and the optical path of the incident light through the multiple reflections of the micro-nano structure is increased [52,53]. At the same time, curve (d) shows that the reflectivity of $Si_{PN}/CN/MoS_x$ is so close to that of Si_{PN}/MoS_x, indicating that the CN coating inserted between Si_{PN} and MoS_x has not adverse effects on the reflectivity of the sample. In addition, the optical band gap of the sample is calculated by using the classical optical absorption relationship [54–57], as shown in Fig. S4. The mean value of E_g (Si) is 1.12 eV, which is consistent with literature reports [14,16]. Meanwhile, we have
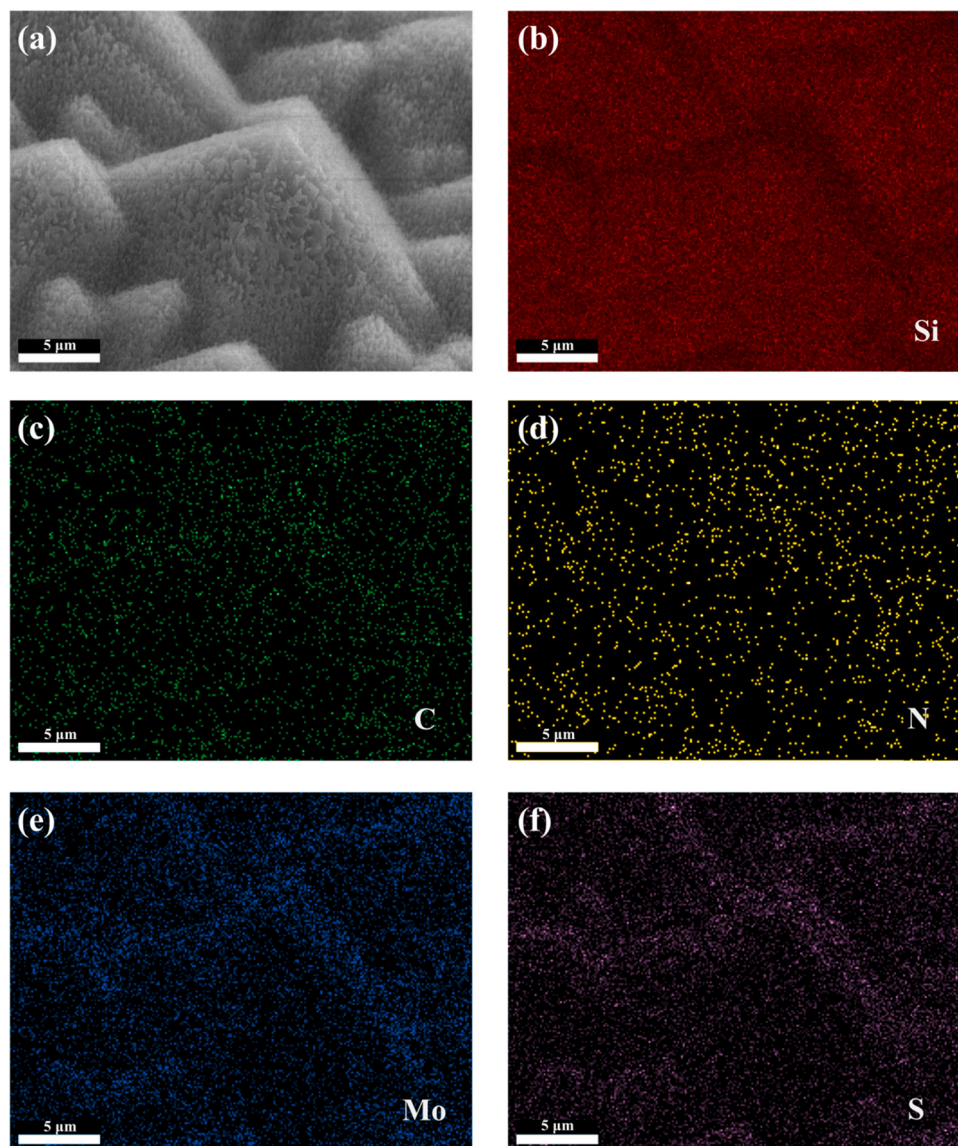
Fig. 3. EDS images of $Si_{PN}/CN/MoS_x$.

utilized the same method to calculate E_g of MoS_x, which is about 1.32 eV.

3.3. Photoelectrochemical behavior and performance

$Si_{PN}/CN/MoS_x$ as a photocathode is used to research PEC performance in 0.5 M H_2SO_4 under AM 1.5 G illumination (100 mW·cm^{-2}). (1) In order to prove the assembly advantage of $Si_{PN}/CN/MoS_x$, the LSVs of $Si_{PN}/CN/MoS_x$, Si_{PN}/MoS_x and Si_{PN} are compared, as shown in Fig. 5a. It can be seen that the photocurrent density (10 mA·cm^{-2}) of $Si_{PN}/CN/MoS_x$ was 2.2 times and 6.5 times that of Si_{PN}/MoS_x and Si_{PN}/CN at 0 V vs RHE. Meanwhile, the onset potential (defined as the potential at −1 mA·cm^{-2}) of $Si_{PN}/CN/MoS_x$ has a more positive value than that of Si_{PN}/MoS_x and Si_{PN}, reaching 0.23 V vs RHE. On one hand, SiO_x may is then generated at the interface of Si_{PN} and MoS_X for Si_{PN}/MoS_x, because, during cathodic deposition, amorphous SiO_2 or H_2SiO_3 is readily formed on the surface of bare Si by oxidation of the electrolyte, which seriously hinders the migration of electrons to the electrode surface [58]. On the other hand, the improved photoelectric performance of $Si_{PN}/CN/MoS_x$ is attributed to that the CN coating facilitates transfer of photogenerated electrons from Si to MoS_x. Meanwhile, the

HER activity of the photocathode is improved by MoS_x. (2) To prove the structural advantage of $Si_{PN}/CN/MoS_x$, the LSVs of $Si_{PN}/CN/MoS_x$, $Si_F/CN/MoS_x$ and $Si_P/CN/MoS_x$ are compared, as shown in Fig. 5b. The photocurrent density of $Si_{PN}/CN/MoS_x$ is 8.4 and 6.6 times of that of $Si_F/CN/MoS_x$ and $Si_P/CN/MoS_x$ at 0 V vs RHE. Because $Si_{PN}/CN/MoS_x$ has excellent anti-reflection ability (seeing Fig. 4f), which can capture more incident light, resulting in more photo-generated carriers. More detailed explanations about the relationship between decreasing light-reflection and increasing photocurrent density have been given in Section 2 of Supplementary Information. Fig. 5c and d show that all photocathodes exhibit sensitive photocurrent response corresponding to the OFF/ON lighting cycle. In addition, the optimization of CN coating and MoS_x attached is shown in Fig. S5.

To better understand the contribution of CN and MoS_x to the photo-generated carrier mobility of $Si_{PN}/CN/MoS_x$ [57], EIS of $Si_{PN}/CN/MoS_x$, Si_{PN}/C_{PDA}, Si_{PN}/MoS_x and Si_{PN} at 0 V vs RHE is compared in 0.5 M H_2SO_4 under AM 1.5 G illumination (100 mW·cm^{-2}), as shown in Fig. 6. The Nyquist plots are fitted according to the equivalent circuit models [59,60], where R_s represents the series resistance, R_{ct2} represents the charge transfer resistance between Si and MoS_x, and R_{ct1} represents the charge transport resistance at the electrode/electrolyte surface. It
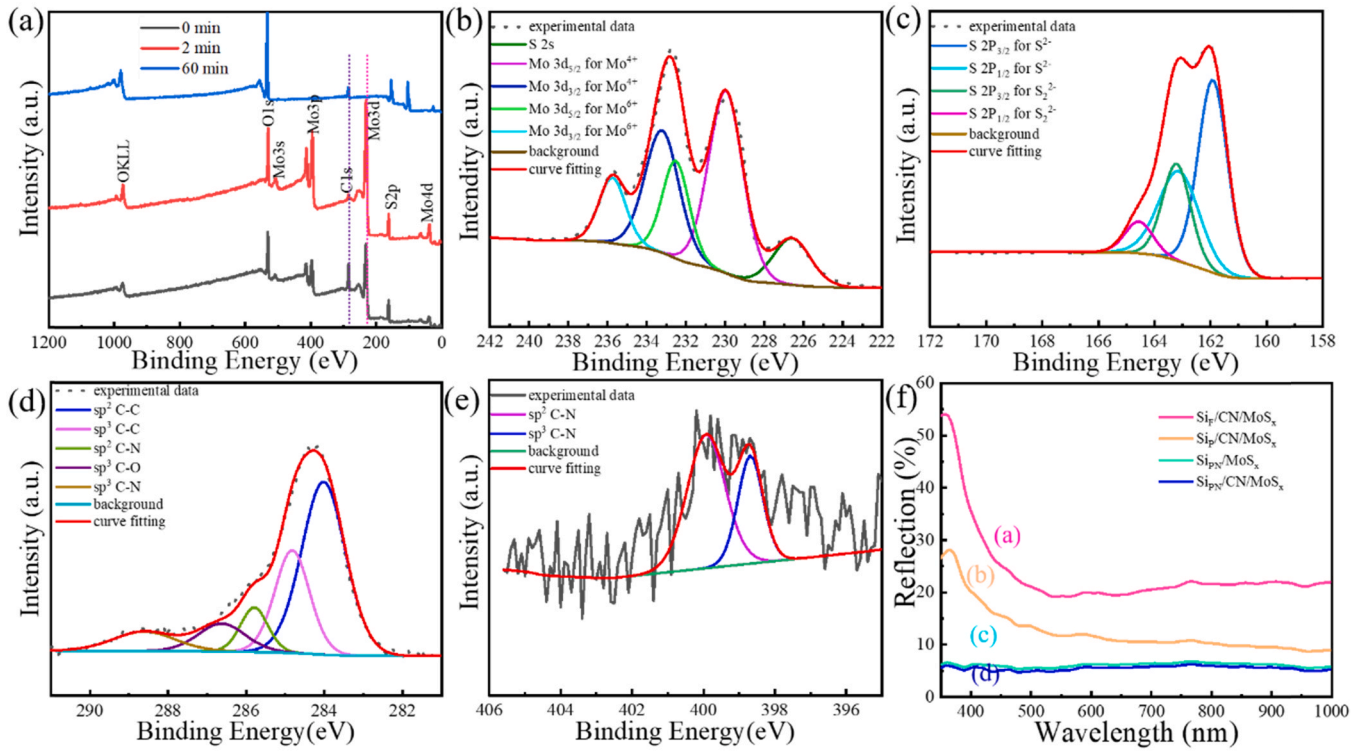
Fig. 4. (a) XPS spectra of $Si_{PN}/CN/MoS_x$ with different etching time. High-resolution XPS spectra of (b) Mo 3d and (c) S 2p without etching, (d) C 1s and (e) N 1s with etching for 60 min (f) Reflectance spectra of $Si_F/CN/MoS_x$, $Si_P/CN/MoS_x$, Si_{PN}/MoS_x and $Si_{PN}/CN/MoS_x$.
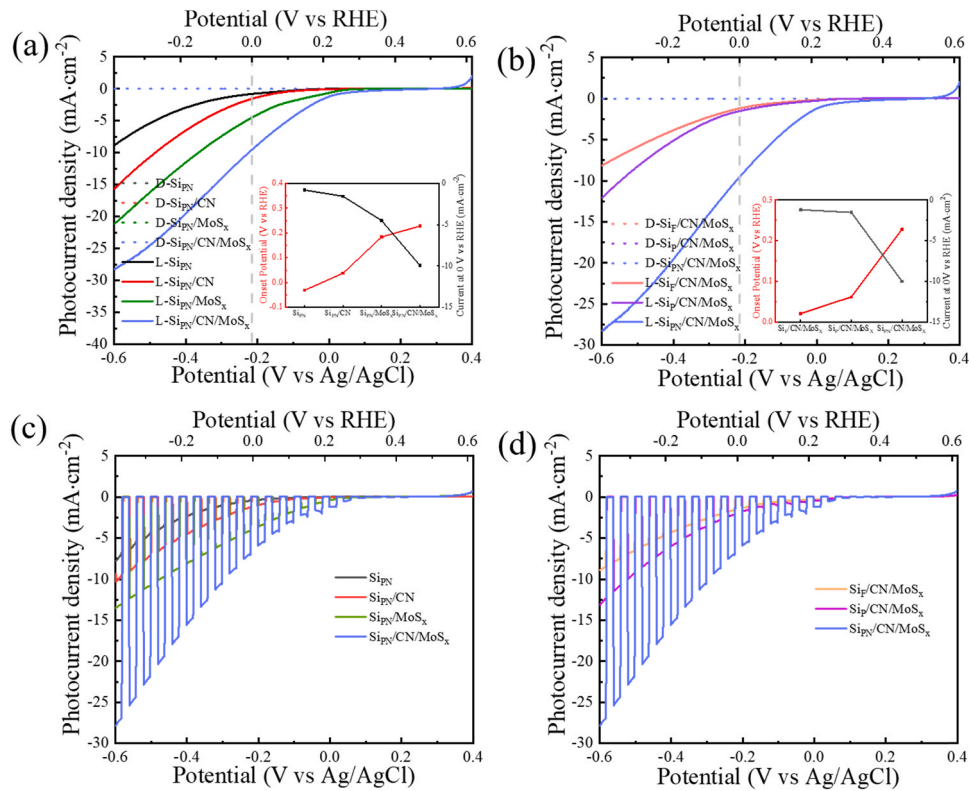

Fig. 5. Linear sweep voltammograms of (a) Si_{PN}, Si_{PN}/CN, Si_{PN}/MoS_x and $Si_{PN}/CN/MoS_x$, (b) $Si_F/CN/MoS_x$, $Si_P/CN/MoS_x$ and $Si_{PN}/CN/MoS_x$ under illumination. The inset maps are the onset potential and photocurrent density at 0 V vs RHE, respectively. Linear sweep voltammograms of (c) Si_{PN}, Si_{PN}/CN, Si_{PN}/MoS_x and $Si_{PN}/CN/MoS_x$, (d) $Si_F/CN/MoS_x$, $Si_P/CN/MoS_x$ and $Si_{PN}/CN/MoS_x$ photocathode under chopping illumination.
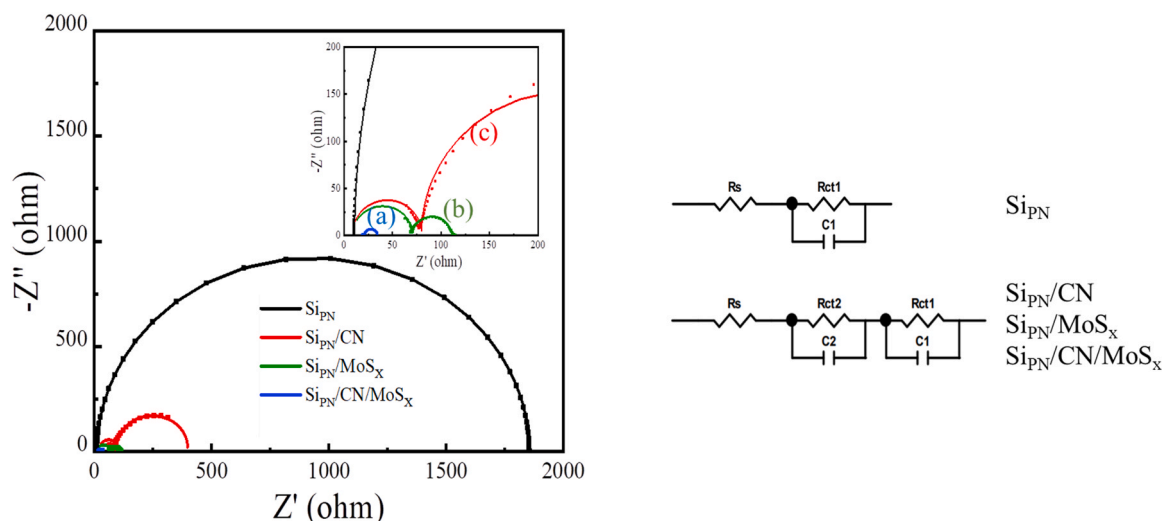
Fig. 6. Nyquist plots of (a) $Si_{PN}/CN/MoS_x$, (b) Si_{PN}/MoS_x, (c) Si_{PN}/CN and (d) Si_{PN} recorded at 0 V vs RHE. Inset: zoomed view in the high-frequency region. The equivalent circuit models for Nyquist plot fitting are shown in the right.

can be seen from the curve (a) that R_s, R_{ct1} and R_{ct2} of $Si_{PN}/CN/MoS_x$ are 17.77 Ω, 13.41 Ω and 2.68 Ω, respectively. Comparing curve (a) with curve (b), R_{ct2} of Si_{PN}/MoS_x is 62.28 Ω far higher than that of $Si_{PN}/CN/MoS_x$, indicating that CN coating can effectively reduce the charge transfer resistance between Si and MoS_x. Comparing curve (a) with curve (c), R_{ct1} of Si_{PN}/CN is 301.40 Ω far higher than that of $Si_{PN}/CN/MoS_x$, indicating that MoS_x can reduce the charge transfer resistance from the electrode surface to the electrolyte. It is worth noting that the Nyquist plot for the Si_{PN} electrode possesses only one impedance semicircle. The Si_{PN} electrode is composed of only one material, resulting that there is only one charge transfer resistance (R_{ct1}) between the electrode and the electrolyte, and no charge transfer resistance (R_{ct2}) between heterogeneous interfaces inside the electrode. The total resistance ($R=R_s + R_{ct1} + R_{ct2}$) is given in the Table S3, according to R ($Si_{PN}/CN/MoS_x$) < R(Si_{PN}/MoS_x) < R(Si_{PN}/CN) < R(Si_{PN}), further illustrating that CN and MoS_x can reduce the charge transfer resistance and increase the HER rate of the electrode/electrolyte interface.

The stability is regarded as an important parameter of photoelectrode. The PEC stability of $Si_{PN}/CN/MoS_x$ and Si_{PN}/MoS_x at 0 V vs RHE in 0.5 MH_2SO_4 was tested by chronoamperometry, as shown in Fig. 7a. The J-t curve shows that the photocurrent density of $SiPN/MoS_x$ is reduced from -6.01 mA·cm^{-2} at 1 h to -1.88 mA·cm^{-2} at 12 h after chronoamperometry test. However, the photocurrent density of $Si_{PN}/CN/MoS_x$ is reduced from -9.64 mA·cm^{-2} at 1 h to -7.16 mA·cm^{-2} at 12 h after chronoamperometry test. It is indicating that the stability of

$Si_{PN}/CN/MoS_x$ is much better than that of $SiPN/MoS_x$. To analyze the reason that the electrochemical stability of $Si_{PN}/CN/MoS_x$ is better than that of Si_{PN}/MoS_x, the binding energy and morphology of MoS_x before and after the chronoamperometry test for 12 h are compared, seeing Fig. 8 and Fig. S6. On the one hand, S_2^{2-} is the active center for HER, which content is proportional to the photocurrent. After the chronoamperometry test for 12 h, as shown in Fig. 8, the atomic ratio of S_2^{2-} to S^{2-} in $Si_{PN}/CN/MoS_x$ and Si_{PN}/MoS_x decreased by 13% and 24%, respectively. This will cause the photocurrent of Si_{PN}/MoS_x to drop much more than that of $Si_{PN}/CN/MoS_x$. On the other hand, the interface compatibility between Si_{PN} and MoS_x in $Si_{PN}/CN/MoS_x$ is better than that in Si_{PN}/MoS_x. In the process of hydrogen escaping from the photoelectrodes, MoS_x on the $Si_{PN}/CN/MoS_x$ surface was almost unchanged after the chronoamperometry test for 12 h, while the MoS_x on the Si_{PN}/MoS_x surface was obviously shed, seeing Fig. S6. In addition, the hydrogen generation of the photocathode was measured by gas chromatography. In Fig. 7b, curves (a), (b) and (c) show the time - dependent actual hydrogen productivities of $Si_{PN}/CN/MoS_x$, $Si_F/CN/MoS_x$ and Si_{PN}/MoS_x, respectively. The hydrogen production rate of $Si_{PN}/CN/MoS_x$ can reach 152.22 μmol·cm^{-2}·h^{-1} within 2 h, which is 2.31 times (65.82 μmol·cm^{-2}·h^{-1}) and 2.09 times (72.72 μmol·cm^{-2}·h^{-1}) than that of $Si_F/CN/MoS_x$ and Si_{PN}/MoS_x, respectively. At the same time, the time - dependent theoretical hydrogen productivities of $Si_{PN}/CN/MoS_x$, $Si_F/CN/MoS_x$ and Si_{PN}/MoS_x are presented by curves (d), (e) and (f) in Fig. 7b, respectively. In the PEC system, when the photoelectrode is
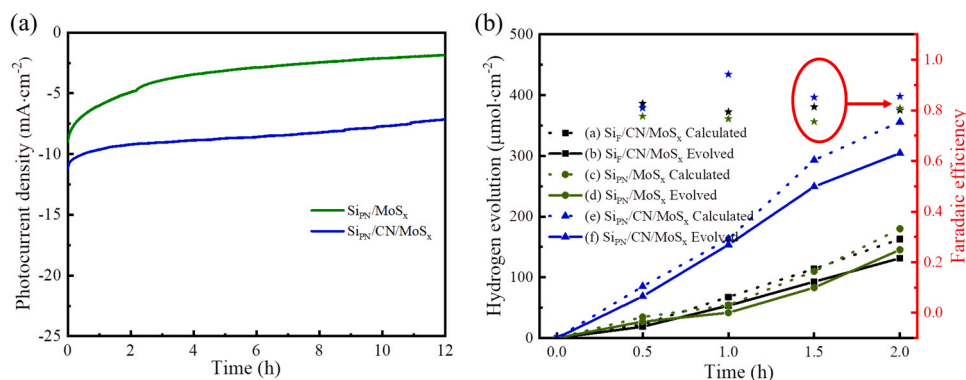

Fig. 7. (a) Chronoamperograms of Si_{PN}/MoS_x and $Si_{PN}/CN/MoS_x$ photocathode at 0 V vs RHE under illumination. (b) Hydrogen evolution of Si_{PN}/MoS_x and $Si_{PN}/CN/MoS_x$ photocathode collected from chronoamperometry measurement within 2 h. The dotted line represents the theoretical calculation, the solid line represents the measured hydrogen production, and the star represents Faradaic efficiency.
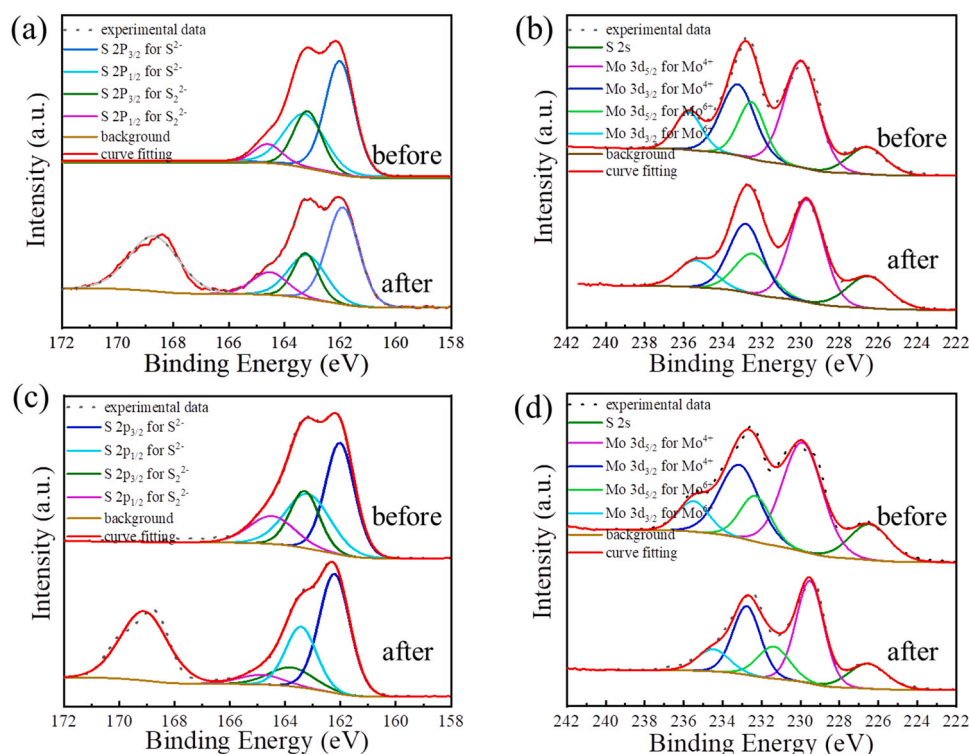
Fig. 8. XPS survey scan spectra before and after chronoamperometry test: (a) S 2p and (b) Mo 3d of $Si_{PN}/CN/MoS_x$ photocathode; (c) S 2p and (d) Mo 3d of Si_{PN}/MoS_x photocathode.

irradiated by sunlight, the monocrystalline Si can absorb the light of <1000 nm and produce photogenerated carriers. Subsequently, the photogenerated carriers are separated under the built-in electric field and/or applied bias voltage, and then transferred to the MoS_x cocatalyst on the electrode surface through the conductive CN layer, which can reduce the transfer resistance of photogenerated electrons. It is well known that MoS_x is an excellent HER catalyst, which can accelerate the HER reaction rate and reduce the overpotential due to the unsaturated S atoms of edge. Therefore, the photogenerated electrons make H^+ in the electrolyte reduce to H_2 on the surface of MoS_x. At the same time, the photogenerated holes are guided by the external current to the counter electrode (Pt), so that H_2O is oxidized to O_2. Combining the actual hydrogen production and the theoretical hydrogen production, Faradaic efficiencies (FE) of $Si_{PN}/CN/MoS_x$, $Si_F/CN/MoS_x$ and Si_{PN}/MoS_x are 85.08%, 80.03% and 80.79%, respectively.

In order to express the relationship between PEC and the incident wavelength, the IPCE measurement was carried out. Fig. 9 shows the
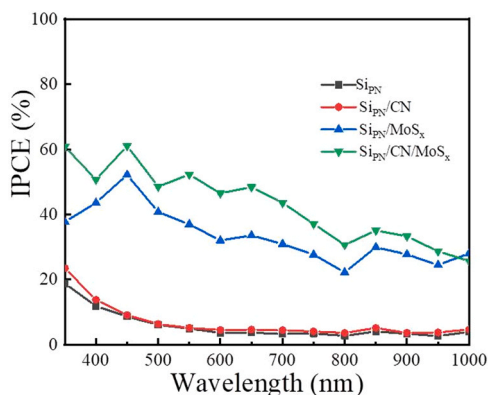

Fig. 9. IPCE of Si_{PN}, Si_{PN}/CN, Si_{PN}/MoS_x and $Si_{PN}/CN/MoS_x$ in the range of 350–1000 nm at 0 V vs RHE.

IPCE spectra of Si_{PN}, Si_{PN}/CN, Si_{PN}/MoS_x and $Si_{PN}/CN/MoS_x$ photoanodes measured with an applied bias potential of 0 V vs RHE in the wavelength region of 350–1000 nm in 0.5 M H_2SO_4 electrolyte. The Si_{PN} and Si_{PN}/CN photocathode show very low IPCE values. The Si_{PN}/MoS_x photoanode show an IPCE value of 30%. After the insertion of a CN layer, the $Si_{PN}/CN/MoS_x$ photoanode shows an enhanced IPCE value of 45%, which is almost 1.5 times than that of the Si_{PN}/MoS_x photoanode. A typical PEC procedure is consisted of three steps (i.e. the production of photon-generated carriers, the migration of photon-generated carriers and the redox reaction of photon-generated carriers on the surface of electrodes.). In this system, Si is used for the generation of photon-generated carriers. The MoS_x (catalyst) layer, which can provide active sites to adsorb H^+/H_3O^+, is used for the reduction reaction of photon-generated carriers and H^+/H_3O^+. The CN layer is a connective layer for Si and MoS_x, and is used to improve the migration efficiency of photon-generated carriers from Si to MoS_x. Therefore, the MoS_x layer and the CN layer play different roles in the $Si_{PN}/CN/MoS_x$ photocathode. As shown in Fig. 9, the IPCE performance of Si_{PN}/CN is worse than Si_{PN}/MoS_x. This is because the catalytic performance of CN is much weaker than MoS_x, which only little carriers take part in the redox reaction of H^+/H_3O^+. The above phenomenon, in combination with the better IPCE performance of $Si_{PN}/CN/MoS_x$ than that of Si_{PN}/MoS_x, further illustrates that the major role of CN layer in the electrode is improving the migration efficiency of carriers and reducing the recombination of carriers.

In addition, the Mott Schottky curve of the electrode was obtained by electrochemical test and then calculated to determine the Fermi level position ($E_{fb} = 0.195$ eV vs NHE) of the $Si_{PN}/CN/MoS_x$ electrode, as shown in Fig. 10a. Whereafter, the position of the valence band ($E_{VB-NHE (si)} = 1.14$ eV and $E_{VB-NHE (MoSx)} = 0.42$ eV) of Si and MoS_x was obtained through XPS test and calculation, as shown in Fig. 10b. In addition, according to the diffuse reflection spectra, the optical band gap width ($E_{g (Si)} = 1.12$ eV and $E_{g (MoSx)} = 1.32$ eV) of Si and MoS_x was calculated by the Kubelka-Munk equation. Finally, the conduction band position ($E_{CB-NHE (Si)} = -0.70$ eV and $E_{CB-NHE (MoSx)} = -0.18$ eV) of Si and MoS_x
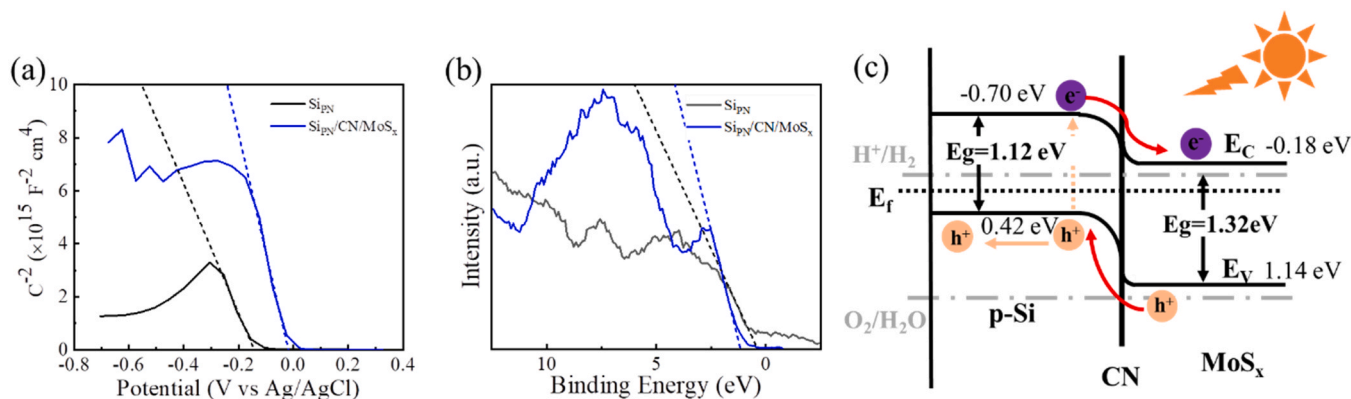
Fig. 10. (a) Electrochemical flat-band potential test of Si_{PN} and $Si_{PN}/CN/MoS_x$. (b) The VB test of the material by XPS. (c) Band arrangement of $Si_{PN}/CN/MoS_x$ photoelectrode and schematic diagram of charge transfer under illumination.

was calculated according to E_{VB-NHE} and E_g. The detailed derivation process is given in Section 3 of Supplementary Information. According to the E_{VB-NHE} and E_{CB-NHE} position of Si and MoS_x, the schematic diagram of charge transfer and separation on the $Si_{PN}/CN/MoS_x$ photocathode involved in the hydrogen evolution reaction has been given in Fig. 10c. As the $Si_{PN}/CN/MoS_x$ electrode is irradiated by incident light, the photogenerated electrons of Si are transferred to the conduction band of MoS_x through CN to carry out the reduction reaction of $H^+ \rightarrow H_2$. Meanwhile, the photogenerated holes of MoS_x are transferred to the valence band of Si and then to the counter electrode (Pt) through the external circuit.

4. Conclusion

In general, we used a simple method of in-situ polymerization and calcination to insert a stability enhanced and conductive C layer between the light absorber Si and the cocatalyst. That is, a PDA coating is formed by in situ polymerization, and a N-doped C layer is formed subsequently by calcination on the surface of the pyramid nanowires silicon wafer. After using a simple electrodeposition method, TMD is deposited on Si to assemble $Si_{PN}/CN/MoS_X$ photoelectrode. The effects of different morphologies and different coatings on the photocatalytic performance were compared from two directions. This study shows that the CN coating acts as a conductive layer, which reduces the charge transfer resistance of the photocathode, thereby promoting the positive transfer of the photoexcited electrons. The N-doped C layer acts as an additional protective layer on the Si photoelectrode to improve the stability of the photocathode in PEC test. The in-situ carbonization of PDA coating on the interface layer between Si and MoS_x is an effective and simple method to improve the electrochemical activity and stability of silicon-based photocathode.

CRediT authorship contribution statement

Shenfeng Zhang: Methodology, Investigation, Validation, Original draft preparation., **Hui Zhao:** Conceptualization, Methodology, Reviewing and Editing., **Xin Li:** Methodology, Investigation, Data curation, Conceptualization., **Ying Li:** Visualization, Reviewing and Editing., **Yuebo Jin** : Methodology., **Xuefeng Liu:** Supervision, Resources. , **Gang Shi:** Supervision, Resources, Conceptualization, Reviewing and editing, Funding acquisition., **Po Keung Wong:** Supervision, Resources, Conceptualization, Reviewing and editing.

Declaration of Competing Interest

The authors declare that they have no known competing financial interests or personal relationships that could have appeared to influence

the work reported in this paper.

Appendix A. Supporting information

Supplementary data associated with this article can be found in the online version at doi:10.1016/j.apcatb.2021.120758.

References

[1] K.T. Fountaine, H.J. Lewerenz, H.A. Atwater, Efficiency limits for photoelectrochemical water-splitting, Nat. Commun. 7 (2016) 13706, https://doi.org/10.1038/ncomms13706.

[2] J. Joy, J. Mathew, S.C. George, Nanomaterials for photoelectrochemical water splitting-review, Int. J. Hydrogen Energy 43 (2018) 4804–4817, https://doi.org/10.1016/j.ijhydene.2018.01.099.

[3] S. Hu, C. Xiang, S. Haussener, A.D. Berger, N.S. Lewis, An analysis of the optimal band gaps of light absorbers in integrated tandem photoelectrochemical water-splitting systems, Energy Environ. Sci. 6 (2013) 2984–2993, https://doi.org/10.1039/c3ee40453f.

[4] D. Bae, B. Seger, P.C.K. Vesborg, O. Hansen, I. Chorkendorff, Strategies for stable water splitting via protected photoelectrodes, Chem. Soc. Rev. 46 (2017) 1933–1954, https://doi.org/10.1039/c6cs00918b.

[5] C. Jiang, S.J.A. Moniz, A. Wang, T. Zhang, J. Tang, Photoelectrochemical devices for solar water splitting-materials and challenges, Chem. Soc. Rev. 46 (2017) 4645–4660, https://doi.org/10.1039/c6cs00306k.

[6] Y. Yang, S. Niu, D. Han, T. Liu, G. Wang, Y. Li, Progress in developing metal oxide nanomaterials for photoelectrochemical water splitting, Adv. Energy Mater. 7 (2017), 1700555, https://doi.org/10.1002/aenm.201700555.

[7] K. Sun, S. Shen, Y. Liang, P.E. Burrows, S.S. Mao, D. Wang, Enabling silicon for solar-fuel production, Chem. Rev. 114 (2014) 8662–8719, https://doi.org/10.1021/cr300459q.

[8] G. Paulraj, P.S. Venkatesh, P. Dharmaraj, S. Gopalakrishnan, K. Jeganathan, Stable and highly efficient MoS_2/Si NWs hybrid heterostructure for photoelectrocatalytic hydrogen evolution reaction, Int. J. Hydrogen Energy 45 (2020) 1793–1801, https://doi.org/10.1016/j.ijhydene.2019.11.051.

[9] R. Fan, G. Huang, Y. Wang, Z. Mi, M. Shen, Efficient n^+p-Si photocathodes for solar H_2 production catalyzed by Co-W-S and stabilized by Ti buffer layer, Appl. Catal. B: Environ. 237 (2018) 158–165, https://doi.org/10.1016/j.apcatb.2018.05.083.

[10] A. Alarawi, V. Ramalingam, H.C. Fu, P. Varadhan, R. Yang, J.H. He, Enhanced photoelectrochemical hydrogen production efficiency of MoS_2-Si heterojunction, Opt. Express 27 (2019) A352–A363, https://doi.org/10.1364/OE.27.00A352.

[11] C.-J. Chen, V. Veeramani, Y.-H. Wu, A. Jena, L.-C. Yin, H. Chang, S.-F. Hu, R.-S. Liu, Phosphorous-doped molybdenum disulfide anchored on silicon as an efficient catalyst for photoelectrochemical hydrogen generation, Appl. Catal. B: Environ. 263 (2020), 118259, https://doi.org/10.1016/j.apcatb.2019.118259.

[12] D. Hu, J. Xiang, Q. Zhou, S. Su, Z. Zhang, X. Wang, M. Jin, L. Nian, R. Nozel, G. Zhou, Z. Zhang, J. Liu, One-step chemical vapor deposition of MoS_2 nanosheets on SiNWs as photocathodes for efficient and stable solar-driven hydrogen

production, Nanoscale 10 (2018) 3518–3525, https://doi.org/10.1039/c7nr09235k.

[13] T.C. Dang, V.T. Dang, T.D. Nguyen, T.H. Truong, M.T. Man, T.T.H. Bui, T.K. C. Tran, D.L. Tran, P.D. Truong, C.K. Nguyen, V.C. Nguyen, D.-B. Seo, E.-T. Kim, MoS$_2$ hydrogen evolution catalysis on p-Si nanorod photocathodes, Mater. Sci. Semicond. Process. 121 (2021), 105308, https://doi.org/10.1016/j.mssp.2020.105308.

[14] L.M. Peter, K.G. Upul Wijayantha, Photoelectrochemical water splitting at semiconductor electrodes: fundamental problems and new perspectives, Chemphyschem 15 (2014) 1983–1995, https://doi.org/10.1002/cphc.201402024.

[15] D. Zhang, J. Shi, W. Zi, P. Wang, S.F. Liu, Recent advances in photoelectrochemical applications of silicon materials for solar-to-chemicals conversion, ChemSusChem 10 (2017) 4324–4341, https://doi.org/10.1002/cssc.201701674.

[16] D. Liu, J. Ma, R. Long, C. Gao, Y. Xiong, Silicon nanostructures for solar-driven catalytic applications, Nano Today 17 (2017) 96–116, https://doi.org/10.1016/j.nantod.2017.10.013.

[17] N. Ali, A. Hussain, R. Ahmed, M.K. Wang, C. Zhao, B.U. Haq, Y.Q. Fu, Advances in nanostructured thin film materials for solar cell applications, Renew. Sustain. Energy Rev. 59 (2016) 726–737, https://doi.org/10.1016/j.rser.2015.12.268.

[18] X. Li, Y. Xiao, J.H. Bang, D. Lausch, S. Meyer, P.T. Miclea, J.Y. Jung, S. L. Schweizer, J.H. Lee, R.B. Wehrspohn, Upgraded silicon nanowires by metal-assisted etching of metallurgical silicon: A new route to nanostructured solar-grade silicon, Adv. Mater. 25 (2013) 3187–3191, https://doi.org/10.1002/adma.201300973.

[19] J.W. Schüttauf, M.A. Modestino, E. Chinello, D. Lambelet, A. Delfino, D. Dominé, A. Faes, M. Despeisse, J. Bailat, D. Psaltis, C. Moser, C. Ballif, Solar-to-hydrogen production at 14.2% efficiency with silicon photovoltaics and earth-abundant electrocatalysts, J. Electrochem. Soc. 163 (2016) F1177–F1181, https://doi.org/10.1149/2.0541610jes.

[20] C. Jian, W. Hong, Q. Cai, J. Li, W. Liu, Surface electron state engineering enhanced hydrogen evolution of hierarchical molybdenum disulfide in acidic and alkaline media, Appl. Catal. B: Environ. 266 (2020), 118649, https://doi.org/10.1016/j.apcatb.2020.118649.

[21] D. Escalera-López, Y. Niu, S.J. Park, M. Isaacs, K. Wilson, R.E. Palmer, N.V. Rees, Hydrogen evolution enhancement of ultra-low loading, size-selected molybdenum sulfide nanoclusters by sulfur enrichment, Appl. Catal. B: Environ. 235 (2018) 84–91, https://doi.org/10.1016/j.apcatb.2018.04.068.

[22] Y. Liu, S. Jiang, S. Li, L. Zhou, Z. Li, J. Li, M. Shao, Interface engineering of (Ni, Fe) S$_2$@MoS$_2$ heterostructures for synergetic electrochemical water splitting, Appl. Catal. B: Environ. 247 (2019) 107–114, https://doi.org/10.1016/j.apcatb.2019.01.094.

[23] Z. Liu, L. Zhao, Y. Liu, Z. Gao, S. Yuan, X. Li, N. Li, S. Miao, Vertical nanosheet array of 1T phase MoS$_2$ for efficient and stable hydrogen evolution, Appl. Catal. B: Environ. 246 (2019) 296–302, https://doi.org/10.1016/j.apcatb.2019.01.062.

[24] J. Hu, B. Huang, C. Zhang, Z. Wang, Y. An, D. Zhou, H. Lin, M.K.H. Leung, S. Yang, Engineering stepped edge surface structures of MoS$_2$ sheet stacks to accelerate the hydrogen evolution reaction, Energy Environ. Sci. 10 (2017) 593–603, https://doi.org/10.1039/c6ee03629e.

[25] R. Fan, J. Mao, Z. Yin, J. Jie, W. Dong, L. Fang, F. Zheng, M. Shen, Efficient and stable silicon photocathodes coated with vertically standing nano-MoS2 films for solar hydrogen production, ACS Appl. Mater. Inter. 9 (2017) 6123–6129, https://doi.org/10.1021/acsami.6b15854.

[26] Y. Shi, Y. Zhou, D.R. Yang, W.X. Xu, C. Wang, F.B. Wang, J.J. Xu, X.H. Xia, H. Y. Chen, Energy level engineering of MoS$_2$ by transition-metal doping for accelerating hydrogen evolution reaction, J. Am. Chem. Soc. 139 (2017) 15479–15485, https://doi.org/10.1021/jacs.7b08881.

[27] Y. Guo, T. Park, J.W. Yi, J. Henzie, J. Kim, Z. Wang, B. Jiang, Y. Bando, Y. Sugahara, J. Tang, Y. Yamauchi, Nanoarchitectonics for transition-metal-sulfide-based electrocatalysts for water splitting, Adv. Mater. 31 (2019), 1807134, https://doi.org/10.1002/adma.201807134.

[28] H. Li, C. Tsai, A.L. Koh, L. Cai, A.W. Contryman, A.H. Fragapane, J. Zhao, H.S. Han, H.C. Manoharan, F. Abild-Pedersen, J.K. Norskov, X. Zheng, Corrigendum: activating and optimizing MoS$_2$ basal planes for hydrogen evolution through the formation of strained sulphur vacancies, Nat. Mater. 15 (2016) 364, https://doi.org/10.1038/nmat4564.

[29] G. Li, C. Fu, J. Wu, J. Rao, S.-C. Liou, X. Xu, B. Shao, K. Liu, E. Liu, N. Kumar, X. Liu, M. Fahlman, J. Gooth, G. Auffermann, Y. Sun, C. Felser, B. Zhang, Synergistically creating sulfur vacancies in semimetal-supported amorphous MoS$_2$ for efficient hydrogen evolution, Appl. Catal. B: Environ. 254 (2019) 1–6, https://doi.org/10.1016/j.apcatb.2019.04.080.

[30] S. Oh, J.B. Kim, J.T. Song, J. Oh, S.-H. Kim, Atomic layer deposited molybdenum disulfide on Si photocathodes for highly efficient photoelectrochemical water reduction reaction, J. Mater. Chem. A 5 (2017) 3304–3310, https://doi.org/10.1039/c6ta10707a.

[31] Q. Ding, F. Meng, C.R. English, M. Caban-Acevedo, M.J. Shearer, D. Liang, A. S. Daniel, R.J. Hamers, S. Jin, Efficient photoelectrochemical hydrogen generation using heterostructures of Si and chemically exfoliated metallic MoS$_2$, J. Am. Chem. Soc. 136 (2014) 8504–8507, https://doi.org/10.1021/ja5025673.

[32] H. Lin, S. Li, G. Yang, K. Zhang, D. Tang, Y. Su, Y. Li, S. Luo, K. Chang, J. Ye, In situ assembly of MoS$_x$ thin-film through self-reduction on p-Si for drastic enhancement of photoelectrochemical hydrogen evolution, Adv. Funct. Mater. 31 (2020), 2007071, https://doi.org/10.1002/adfm.202007071.

[33] P.D. Tran, S.S. Pramana, V.S. Kale, M. Nguyen, S.Y. Chiam, S.K. Batabyal, L. H. Wong, J. Barber, J. Loo, Novel assembly of an moS$_2$ electrocatalyst onto a silicon nanowire array electrode to construct a photocathode composed of elements

[34] D.W. Redman, H.J. Kim, K.J. Stevenson, M.J. Rose, Photo-assisted electrodeposition of MoS$_x$ from ionic liquids on organic-functionalized silicon photoelectrodes for H$_2$ generation, J. Mater. Chem. A 4 (2016) 7027–7035, https://doi.org/10.1039/c5ta09684g.

[35] B. Seger, D.S. Tilley, T. Pedersen, P.C.K. Vesborg, O. Hansen, M. Grätzel, I. Chorkendorff, Silicon protected with atomic layer deposited TiO$_2$: durability studies of photocathodic H$_2$ evolution, RSC Adv. 3 (2013) 25902, https://doi.org/10.1039/c3ra45966g.

[36] C.W. Roske, E.J. Popczun, B. Seger, C.G. Read, T. Pedersen, O. Hansen, P. C. Vesborg, B.S. Brunschwig, R.E. Schaak, I. Chorkendorff, H.B. Gray, N.S. Lewis, Comparison of the performance of CoP-coated and Pt-Coated radial junction n(+) p-silicon microwire-array photocathodes for the sunlight-driven reduction of water to H$_2$(g), J. Phys. Chem. Lett. 6 (2015) 1679–1683, https://doi.org/10.1021/acs.jpclett.5b00495.

[37] B. Seger, A.B. Laursen, P.C.K. Vesborg, T. Pedersen, O. Hansen, S. Dahl, I. Chorkendorff, Hydrogen production using a molybdenum sulfide catalyst on a titanium-protected n$^+$p-silicon photocathode, Angew. Chem. Int. Ed. 51 (2012) 9128–9131, https://doi.org/10.1002/anie.201203585.

[38] Y. Li, L. Feng, J. Li, X. Li, J. Chen, L. Wang, D. Qi, X. Liu, G. Shi, Fabrication of an insect-like compound-eye SERS substrate with 3D Ag nano-bowls and its application in optical sensor, Sens. Actuators B: Chem. 330 (2021), 129357, https://doi.org/10.1016/j.snb.2020.129357.

[39] J. Chen, D. Wang, X. Li, H. Sun, H. Zhao, Y. Li, X. Liu, G. Shi, Photothermal membrane of CuS/polyacrylamide-carboxymethyl cellulose for solar evaporation, ACS Appl. Polym. Mater. 3 (2021) 2402–2410, https://doi.org/10.1021/acsapm.0c01422.

[40] Y. Wang, L. Feng, H. Zhu, H. Miao, Y. Li, X. Liu, G. Shi, Noncontact metal-spiropyran-metal nanostructured substrates with Ag and Au@SiO$_2$ nanoparticles deposited in nanohole arrays for surface-enhanced fluorescence and trace detection of metal ions, ACS Appl. Nano Mater. 4 (2021) 3780–3789, https://doi.org/10.1021/acsanm.1c00225.

[41] Q. Yang, L. Liu, L. Xiao, L. Zhang, M.J. Wang, J. Li, Z. Wei, Co$_9$S$_8$@N,S-codoped carbon core-shell structured nanowires: constructing a fluffy surface for high-density active sites, J. Mater. Chem. A. 6 (2018) 14752–14760, https://doi.org/10.1039/c8ta03604g.

[42] J. Gu, J.A. Aguiar, S. Ferrere, K.X. Steirer, Y. Yan, C. Xiao, J.L. Young, M. Al-Jassim, N.R. Neale, J.A. Turner, A graded catalytic-protective layer for an efficient and stable water-splitting photocathode, Nat. Energy 2 (2017) 1–8, https://doi.org/10.1038/nenergy.2016.192.

[43] S.S. Kalanur, I.-H. Yoo, I.-S. Cho, H. Seo, Effect of oxygen vacancies on the band edge properties of WO$_3$ producing enhanced photocurrents, Electrochim. Acta 296 (2019) 517–527, https://doi.org/10.1016/j.electacta.2018.11.061.

[44] X. Long, X. Gao, F. Li, Y. Hu, S. Wei, C. Wang, T. Wang, J. Jin, J. Ma, Bamboo shoots shaped FeVO$_4$ passivated ZnO nanorods photoanode for improved charge separation/transfer process towards efficient solar water splitting, Appl. Catal. B: Environ. 257 (2019), 117813, https://doi.org/10.1016/j.apcatb.2019.117813.

[45] G. Shi, J. Chen, L. Wang, D. Wang, J. Yang, Y. Li, L. Zhang, C. Ni, L. Chi, Titanium oxide/silicon moth-eye structures with antireflection, p-n heterojunctions, and superhydrophilicity, Langmuir 32 (2016) 10719–10724, https://doi.org/10.1021/acs.langmuir.6b03117.

[46] X. Jin, Q. Zhu, L. Feng, X. Li, H. Zhu, H. Miao, Z. Zeng, Y. Wang, Y. Li, L. Wang, X. Liu, G. Shi, Light-trapping SERS substrate with regular bioinspired arrays for detecting trace dyes, ACS Appl. Mater. Int. 13 (2021) 11535–11542, https://doi.org/10.1021/acsami.1c00702.

[47] X. Li, F. Wu, Y. Jin, D. Zhai, Y. Li, C. Ni, G. Shi, Efficient gatherer of sunlight based on two-sided bio-inspired antireflective micro-pyramids with PPy/TiO$_2$, Inorg. Chem. Commun. 110 (2019), 107604, https://doi.org/10.1016/j.inoche.2019.107604.

[48] H. Zhao, C. Tian, J. Mei, S. Yang, P.K. Wong, Synergistic effect and mechanism of catalytic degradation toward antibiotic contaminants by amorphous goethite nanoparticles decorated graphitic carbon nitride, Chem. Eng. J. 390 (2020), 124551, https://doi.org/10.1016/j.cej.2020.124551.

[49] H. Vrubel, D. Merki, X. Hu, Hydrogen evolution catalyzed by MoS$_3$ and MoS$_2$ particles, Energy Environ. Sci. 5 (2012) 6136–6144, https://doi.org/10.1039/c2ee02835b.

[50] H. Wang, Z. Lu, D. Kong, J. Sun, T.M. Hymel, Y. Cui, Electrochemical tuning of MoS$_2$ nanoparticles on three-dimensional substrate for efficient hydrogen evolution, ACS Nano 8 (2014) 4940–4947, https://doi.org/10.1021/nn500959v.

[51] T. Wang, L. Liu, Z. Zhu, P. Papakonstantinou, J. Hu, H. Liu, M. Li, Enhanced electrocatalytic activity for hydrogen evolution reaction from self-assembled monodispersed molybdenum sulfidenanoparticles on an Au electrode, Energy Environ. Sci. 6 (2013) 625–633, https://doi.org/10.1039/c2ee23513g.

[52] G. Shi, X. Zhang, J. Li, H. Zhu, Y. Li, L. Zhang, C. Ni, L. Chi, Fabrication of 3D biomimetic composite coating with broadband antireflection, superhydrophilicity, and double p-n heterojunctions, Nano Res 10 (2017) 2377–2385, https://doi.org/10.1007/s12274-017-1434-5.

[53] X. Li, Y. Li, H. Wang, H. Miao, H. Zhu, X. Liu, H. Lin, G. Shi, Fabrication of a three-dimensional bionic Si/TiO$_2$/MoS$_2$ photoelectrode for efficient solar water splitting, ACS Appl. Energy Mater. 4 (2021) 730–736, https://doi.org/10.1021/acsaem.0c02594.

[54] S. Chen, Y. Hu, S. Meng, X. Fu, Study on the separation mechanisms of photogenerated electrons and holes for composite photocatalysts g-C$_3$N$_4$-WO$_3$, Appl. Catal. B: Environ. 150 151 (2014) 564–573, https://doi.org/10.1016/j.apcatb.2013.12.053.

[55] K. Dai, L. Lu, C. Liang, Q. Liu, G. Zhu, Heterojunction of facet coupled g-C$_3$N$_4$/ surface-fluorinated TiO$_2$ nanosheets for organic pollutants degradation under visible LED light irradiation, Appl. Catal. B: Environ. 156–157 (2014) 331–340, https://doi.org/10.1016/j.apcatb.2014.03.039.

[56] X. Yang, F. Qian, G. Zou, M. Li, J. Lu, Y. Li, M. Bao, Facile fabrication of acidified g-C$_3$N$_4$/g-C$_3$N$_4$ hybrids with enhanced photocatalysis performance under visible light irradiation, Appl. Catal. B: Environ. 193 (2016) 22–35, https://doi.org/10.1016/j.apcatb.2016.03.060.

[57] I.-H. Yoo, Y.-J. Lee, S.S. Kalanur, H. Seo, Assembly of nonstoichiometric molybdenum oxide on Si as p-n junction photocathode for enhanced hydrogen evolution, Appl. Catal. B: Environ. 264 (2020), 118542, https://doi.org/10.1016/j.apcatb.2019.118542.

[58] Z. Luo, T. Wang, J. Gong, Single-crystal silicon-based electrodes for unbiased solar water splitting: current status and prospects, Chem. Soc. Rev. 48 (2019) 2158–2181, https://doi.org/10.1039/C8CS00638E.

[59] S. Zhou, S. Wang, S. Zhou, H. Xu, J. Zhao, J. Wang, Y. Li, An electrochromic supercapacitor based on an MOF derived hierarchical-porous NiO film, Nanoscale 12 (2020) 8934–8941, https://doi.org/10.1039/D0NR01152E.

[60] Y. Li, F. Wu, X. Jin, H. Xu, X. Liu, G. Shi, Preparation and electrochemical properties of graphene quantum dots/biomass activated carbon electrodes, Inorg. Chem. Commun. 112 (2020), 107718, https://doi.org/10.1016/j.inoche.2019.107718.